Bulky End-Capped [1]Benzothieno[3,2-*b*]benzothiophenes: Reaching High-Mobility Organic Semiconductors by Fine Tuning of the Crystalline Solid-State Order

Guillaume Schweicher, Vincent Lemaur, Claude Niebel, Christian Ruzié, Ying Diao, Osamu Goto, Wen-Ya Lee, Yeongin Kim, Jean-Baptiste Arlin, Jolanta Karpinska, Alan R. Kennedy, Sean R. Parkin, Yoann Olivier, Stefan C. B. Mannsfeld, Jérôme Cornil, Yves H. Geerts, and Zhenan Bao**

For the past two decades, organic electronics has emerged as a field of intense research gaining considerable industrial interest due to its potential revolutionary applications such as flexible displays and sensors.[1] In spite of tremendous progress in molecular design, engineering, and processing, only a few small molecule organic semiconductors (OSCs) have reached field-effect mobilities higher than 10 $cm^2\ V^{-1}\ s^{-1}$, typically with single-crystal devices.[2] Moreover, as a result of the anisotropic nature of charge transport in these weakly van der Waals bounded systems, preferential alignment along the highest charge transport axis is necessary to harvest the full potential of single crystals.[3,4] However, uniform and large-area production of single crystals with controlled size, shape, and orientation at designated locations on a substrate remains challenging and hampers their use for practical applications.[4,5]

Dr. G. Schweicher, Dr. Y. Diao, Dr. O. Goto, Dr. W.-Y. Lee, Y. Kim, Prof. Z. Bao
Department of Chemical Engineering
Stanford University
381 North-South Mall, Stanford, CA 94305, USA
E-mail: zbao@stanford.edu
Dr. V. Lemaur, Dr. Y. Olivier, Dr. J. Cornil
Laboratory for Chemistry of Novel Materials
University of Mons
Place du Parc 20, B-7000 Mons, Belgium
Dr. C. Niebel, Dr. C. Ruzié, Dr. J.-B. Arlin, Dr. J. Karpinska, Prof. Y. H. Geerts
Laboratoire de Chimie des Polymères
Faculté des Sciences
Université Libre de Bruxelles (ULB)
CP206/1, Boulevard du Triomphe, 1050 Brussels, Belgium
E-mail: ygeerts@ulb.ac.be
Dr. A. R. Kennedy
Department of Pure and Applied Chemistry
University of Strathclyde
295 Cathedral Street, Glasgow G1 1XL, UK
Dr. S. R. Parkin
Department of Chemistry
University of Kentucky
Lexington, KY 40506-0055, USA
Prof. S. C. B. Mannsfeld
Center for Advancing Electronics Dresden
Technische Universität Dresden
01062 Dresden, Germany

DOI: 10.1002/adma.201500322

The large body of work on OSCs developed over the years provides us with clues for the rational design of new promising small molecule materials. The excellent performance of rubrene and 6,13-bis(triisopropylsilylethynyl)pentacene (TIPS-pentacene) comes from their respective 2D layered herringbone and brickwall packing, as a result of the steric hindrance of the bulky substituents.[6] However, their packing structures also give rise to pronounced in-plane charge transport anisotropy.[7]

Among the reported molecular semiconductors, [1]benzothieno[3,2-*b*]benzothiophene (BTBT)[8] and dinaphtho[2,3-*b*:2′,3′-*f*]thieno[3,2-*b*]thiophene (DNTT)[9] have shown some of the highest mobilities reported to date.[4,10] Combined with a high chemical stability and an easy synthetic route, these molecules are attractive core units for structure–property relationship studies. Moreover, multiple successful derivatization attempts of these aromatic cores have already been reported in the literature.[11] It is also worth mentioning the brand new promising V- and N-shaped materials developed by Okamoto et al.[12]

In a previous study, the Bao group demonstrated the ability to modify charge transport properties of oligothiophenes via fine tuning of their crystal packing structures by the addition of bulky pendant groups.[13] This gave rise to a rationally designed OSC, trimethyl-[2,2′;5′,2″;5″,2‴]quaterthiophen-5-yl-silane (4TTMS), which has an in-plane isotropic mobility of 0.1 $cm^2\ V^{-1}\ s^{-1}$ recorded with physical vapor transport (PVT) grown single-crystal organic field-effect transistors (OFETs).[14]

In this Communication, we report the substitution of the BTBT core with end groups of different bulkiness in an attempt to modulate the charge transport properties of the resulting materials through changing the molecular packing lattice in the *x,y* herringbone plane in order to potentially achieve high charge carrier mobility above 10 $cm^2\ V^{-1}\ s^{-1}$. This work allowed us to identify 2,7-di-*tert*-butylBTBT (**ditBu-BTBT**) as a new high-performance OSC with large and well-balanced transfer integrals, as evidenced by quantum-chemical calculations. Single-crystal FETs showed a remarkable average saturation mobility of 7.1 $cm^2\ V^{-1}\ s^{-1}$ (maximum mobility of 17 $cm^2\ V^{-1}\ s^{-1}$) while solution processed thin films showed an average mobility of 2.4 $cm^2\ V^{-1}\ s^{-1}$ (maximum mobility of 3.7 $cm^2\ V^{-1}\ s^{-1}$).

The chemical structures of the investigated molecules are classified by ascending order of bulkiness: mono-isopropyl **iPr**, di-isopropyl **diiPr**, mono-tertbutyl **tBu**, di-tertbutyl **ditBu**, bis(trimethylsilyl) **diTMS** (**Figure 1**a). The full synthetic

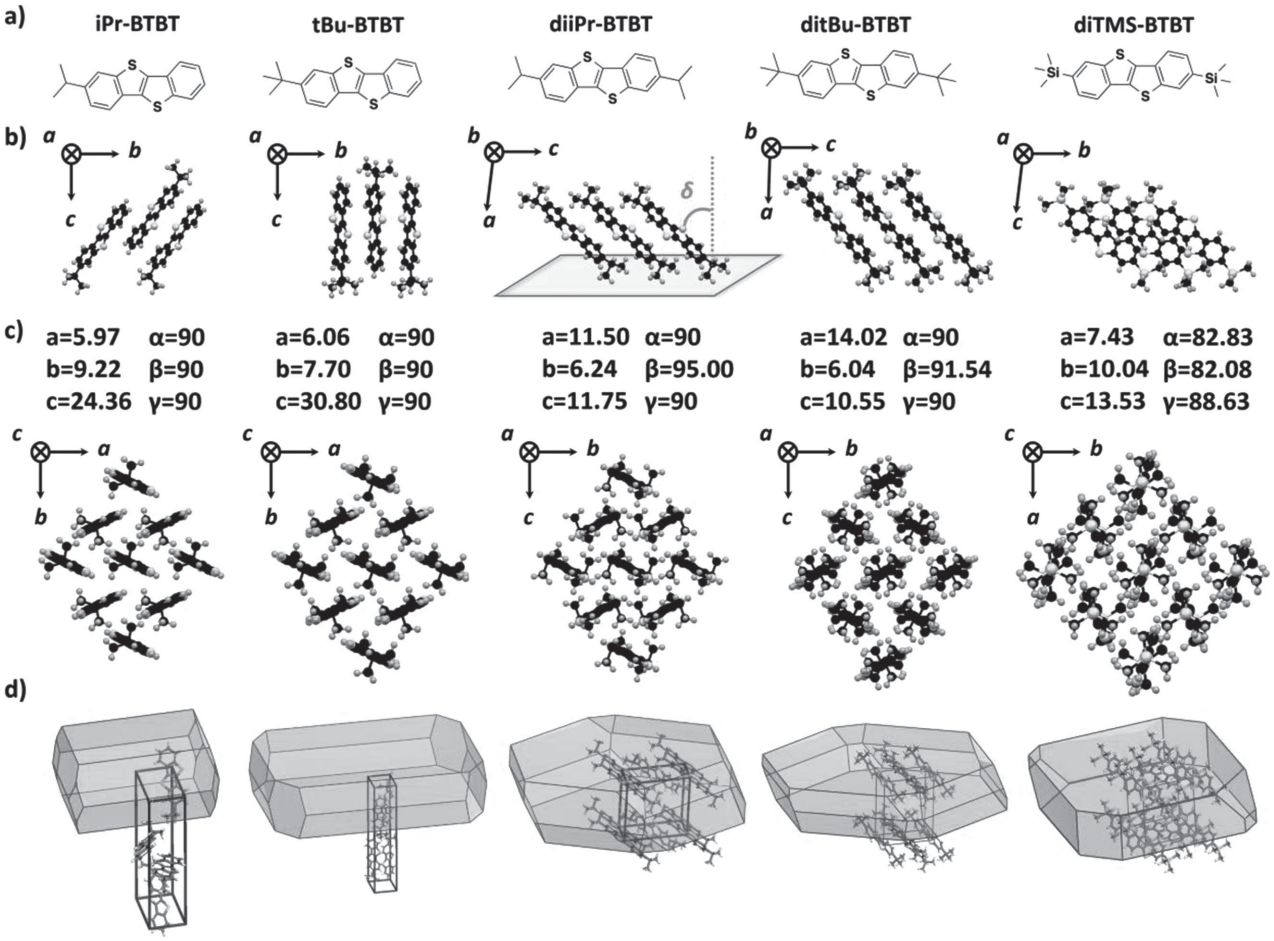

Figure 1. a) Molecular structure of the different bulky end-capped BTBTs classified by ascending order of bulkiness. b) Side view of the lamellar herringbone packing structure. Terminal substitution determines the in-plane tilt (δ) of the BTBT cores, with **diTMS-BTBT** (51.3°) > [**diiPr-BTBT** (42.5°) - **iPr-BTBT** (35.8°)] > [**ditBu-BTBT** (40.5°) - **tBu-BTBT** (0°)]. c) Lattice parameters and top view of the lamellar herringbone packing structure. d) Calculated crystal growth morphology of the different BTBTs.

procedures are detailed in the Supporting Information. The thermal behavior of the different BTBTs was investigated by thermogravimetric analysis (TGA) and differential scanning calorimetry (DSC).

Sublimation and/or evaporation of the materials occurs at temperatures ranging from 260 to 290 °C (Figure S1a, Supporting Information), giving access to easy vacuum sublimation purification and vapor growth of single crystals. DSC traces as well as transition temperatures and their associated energies are presented in Figure S1b and Table S1 (Supporting Information). **ditBu-BTBT** and **diTMS-BTBT** show the highest melting points (277.1 and 215.3 °C, respectively) with a crystal–crystal transition at lower temperatures (71.2 and 154.7 °C, respectively). Interestingly, the TMS substitution of the aromatic core gives rise to an almost 80 °C increase in the reversible crystal–crystal transition (Figure S1c,d, Supporting Information). On the other hand, it also reduces the close molecular packing, as observed by the 60 °C decrease of the melting point.

Single crystals of the different BTBT derivatives were grown by PVT (growth parameters are presented in Table S2, Supporting Information) in order to investigate their molecular packing and charge transport properties. Structure determination was realized by single-crystal X-ray diffraction and the complete crystal data are available in Table S3 (Supporting Information). The bulky end-capped BTBTs adopt a standard layer-by-layer herringbone packing motif with a tilt angle of the molecules within a herringbone layer, δ, being determined by the terminal substitution (Figure 1b; the tilt angle of the molecule is defined as the angle between the plane of the aromatic core and the direction normal to the herringbone layer plane). Indeed, the bulkiness of the TMS substitution imposes a severe tilt on the molecules (51.3°) while the tilt is reduced for iPr substitution [**diiPr-BTBT** (42.5°) – **iPr-BTBT** (35.8°)] and even more reduced for the tBu-derivatives [**ditBu-BTBT** (40.5°) – **tBu-BTBT** (0°)]. We attribute the tilt angle observed for the iPr compounds to their asymmetry and reduced bulkiness, inducing more disorder and allowing interactions with the neighboring layers (**iPr-BTBT**). Monosubstituted aromatic cores present an alternating upside down arrangement of the molecules, allowing the cores to arrange more vertically (smaller tilt angle compared to disubstituted derivatives). Moreover, both asymmetric compounds also possess a higher crystalline symmetry (orthorhombic vs monoclinic

for **diiPr-BTBT** and **ditBu-BTBT** and triclinic for **diTMS-BTBT**). Finally, it is worth mentioning that both **tBu-BTBT** and **diiPr-BTBT** crystals possess certain amounts of disorder (see Figure S2, Supporting Information) in their molecular packing that could have a direct impact on their charge transport properties, as will be explained later. Crystallographic information files (CIFs) for the different BTBT derivatives are summarized in the Supporting Information (these data can also be obtained free of charge from The Cambridge Crystallographic Data Centre; 1008118 (**tBu-BTBT**), 1008119 (**iPr-BTBT**), 1008120 (**diiPr-BTBT**), 1008575 (**ditBu-BTBT**), and 1008576 (**diTMS-BTBT**)). Grazing-incidence X-ray diffraction (GIXD) performed at room temperature on thin-platelet single crystals of **ditBu-BTBT** grown by PVT (laminated on a silicon substrate) confirmed their molecular packing in the monoclinic phase (Figure S3 and Table S4 (Supporting Information), also including powder diffractograms and refined parameters achieved through specular X-ray diffraction (sXRD) of a powder sample).

In order to have a clear quantitative and visual insight into the intermolecular interactions, Hirshfeld surfaces of the bulky end-capped BTBTs and their relative 2D fingerprints were calculated using Crystal Explorer (Figure S4, Supporting Information). Interestingly, the ditBu substitution of the BTBT core induces a deformation of the molecular packing, leading to the absence of any dominant interactions, which can be seen in the Hirshfeld surfaces as the bright red areas. All the other BTBT derivatives as well as **C12-BTBT**, used for comparison, present a molecular packing impacted by the dominant S···S and/or C···S interactions (H···S in the case of **diTMS-BTBT**). A look at the percentage contributions of the various close intermolecular contacts for the different BTBT derivatives (Figure S5, Supporting Information) highlights the effect of the bulkiness of the ditBu and diTMS substitutions, hampering the contribution of the S···S and C···S interactions on the resulting molecular packing. The sum of their contributions reaches 7% in the case of **ditBu-BTBT**, while the bulkier **diTMS-BTBT** only provides a contribution of 3.8% (other bulky end-capped BTBTs show values ranging from 9.9% to 15.7% while the contribution in **C12-BTBT** is 6.7%). As recently reported by Kreyes et al., the bulkiest investigated substitution, diTMS, is expected to have a more detrimental effect on the charge transport properties of the material.[15] Indeed, such a substitution clearly increases the distance between neighboring molecules within the 2D in-plane herringbone packing.

All the compounds formed extremely thin, nearly 2D platelet crystals, ideal for single-crystal transistor device fabrication except **iPr-BTBT**, which favored the growth of needles. The observed crystal habits clearly fit their crystal growth morphologies calculated by the Hartman theory, and are visible in Figure 1d (a detailed indexation of the attachment energies and corresponding percentage in the total facet area of the most dominant faces in the growth morphology is presented in Table S5, Supporting Information).[16] **iPr-BTBT**, with its stronger out-of-plane interactions opens the way for acicular growth, as observed by the formation of thick needle-like single crystals. Lower performances are expected for devices built from the thick crystals of this material as a result of the higher access resistance, which is the resistance related to the pass of the charge carriers from the electrode, on top of the organic single crystal, down to the accumulation layer.[17,18] Moreover, it is worth noting that the flatter disk-like morphology observed for **ditBu-BTBT** is likely the result of its almost uniform in-plane interactions.

Figure 2 presents the most important energetic parameters relative to the charge transport properties of our BTBT derivatives in a hopping regime: the reorganization energy (λ), the transfer integral (J), and the ionization potential (IP); note that the hopping regime is a good starting point to model charge transport in devices operating at room temperature due to the localization of the charge carriers induced by lattice thermal fluctuations.[19] The reorganization energies and transfer integrals between the highest occupied molecular orbitals (HOMOs) of the individual

a)

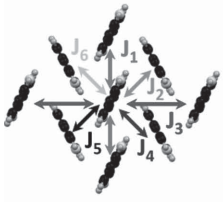

Compound	J_1 [meV]	J_2 [meV]	J_3 [meV]	J_4 [meV]	J_5 [meV]	J_6 [meV]
iPr-BTBT	58	11	0.3	11	21	21
tBu-BTBT	35	14	0.4	16	16	14
diiPr-BTBT	57	35	0.2	35	35	35
ditBu-BTBT	60	53	0.2	53	53	53
diTMS-BTBT	2	43	1	37	43	37

b)

Compound	Ionization potential [eV]	λ_{i+} [eV]	μ_{max} [$cm^2 V^{-1} s^{-1}$]	μ [$cm^2 V^{-1} s^{-1}$]	V_{th} [V]	I_{on}/I_{off}
iPr-BTBT	5.8	0.24	0.08	0.04±0.04	-100.0±15.6	$2.1\ 10^5$
tBu-BTBT	5.5	0.24	2.1	0.4±0.6	-68.5±5.5	$1.6\ 10^7$
diiPr-BTBT	5.6	0.24	/	/	/	/
ditBu-BTBT	5.7	0.25	17.0	7.1±4.0	-71.0±5.7	$3.0\ 10^9$
diTMS-BTBT	5.6	0.29	0.6	0.3±0.1	-88.2±7.4	$1.0\ 10^7$

Figure 2. a) Top view of the lamellar herringbone packing structure with DFT-calculated transfer integrals. b) Performances of PVT grown single crystals of the different BTBT derivatives extracted from 3, 10, 5, 42, and 5 devices, respectively.

units were calculated at the density functional theory (DFT) level; see the Experimental Section. The reorganization energies are very close for the different bulky end-capped BTBTs and range between 0.24 and 0.29 eV (Table S6, Supporting Information), the highest value being obtained for **diTMS-BTBT**. The calculated transfer integral values point to a strong electronic overlap of the HOMO levels, with marked differences among the interacting dimers depending on substituents. These variations are critical and have to be as small as possible in order to approach isotropic charge transport properties. **ditBu-BTBT** presents large and well-balanced transfer integrals in the plane (60 meV, 53 meV, 12% deviation) compared to the other derivatives. Moreover, these values are larger and more balanced compared to those achieved for the well-known high-performance **C12-BTBT** (56 meV, 43 meV, 23% deviation). The anisotropy of the field-effect mobility in a pure hopping regime has been calculated with a kinetic Monte Carlo approach (see the Experimental Section) as a function of the crystal packing for the different OSCs and is presented in Figure S6 (Supporting Information). As expected, these plots highlight the relative anisotropy of charge transport in the different derivatives and in particular the very interesting and almost perfect isotropic transport achieved in **ditBu-BTBT** (**Figure 3**g). It is worth mentioning that all those calculations have been performed on structures solved at low temperature and can be affected to some extent by the thermal expansion and the dynamic of the system.[20] Finally, the IPs were measured by photoelectron spectroscopy on thin films spin coated (10 mg mL^{-1} in chlorobenzene – thickness ranging from 60 to 90 nm) on glass substrates. The IPs of the different BTBT derivatives, ranging from 5.5 to 5.8 eV, are presented in Figure 2b. The large variation in IP levels as a function of molecular packing highlights the strong effect of molecular packing on solid-state electronic polarization effects.[21] The extremely deep values of the experimental IPs are required to use a top-contact OFET configuration with the application of a MoO_3 hole-injection layer (electron affinity goes from –6.7 eV for a freshly evaporated layer till –5.2 eV after exposure to moisture present in the air).[22]

Single-crystal charge transport properties of the bulky end-capped BTBTs were evaluated by using thin platelet PVT-grown crystals. Transistors were fabricated by evaporation of a MoO_3 layer and Au electrodes through a shadow mask on top of the single crystals laminated on octadecyltrimethoxysilane (OTS) treated 300 nm thermally grown SiO_2 substrates. The resulting bottom-gate top-contact device architecture is presented in Figure 3a. In order to avoid any loss of performance due to the exposure of MoO_3 to the atmosphere, devices were directly transferred to a N_2-filled glovebox (after electrodes evaporation) before subsequent measurements.

The FET performances in terms of hole transport are presented in Figure 2b. At first sight, it is clear that the performances are directly impacted by the deep IPs of our materials whose devices present non-idealities and large V_{th} values combined with low mobilities (OFETs characteristics of the different BTBT derivatives are presented in Figure S7, Supporting Information).[23] As a result, mobility extractions have been realized over a reduced range of gate voltages, typically 10 to 20 V (in order to take into account the presence of a small mobility dependence as a function of the gate voltage as highlighted in Figure S7, Supporting Information). Moreover, the structural disorder present in **tBu-BTBT** and **diiPr-BTBT** demonstrates its propensity to impede charge transport, as evidenced by the poor performance of **tBu-BTBT** devices and our inability to record any FET response for **diiPr-BTBT**. However, **ditBu-BTBT** clearly demonstrates its potential with saturation mobility up to 17 $cm^2\ V^{-1}\ s^{-1}$ (average 7.1 $cm^2\ V^{-1}\ s^{-1}$) accompanied by a very high on/off ratio of 10^9 (Figure 3b–d shows the optical microscopy image and OFET characteristics of a **ditBu-BTBT** device presenting a field-effect mobility of 17 $cm^2\ V^{-1}\ s^{-1}$). As a result of the top-contact geometry, together with the deep IPs and higher hole-injection barriers, our mobility distribution is directly related to the thickness distribution of the selected single crystals used to fabricate the devices (the importance of the strong acceptor in the contacts is presented in the Supporting Information with results obtained using only Au and another strong acceptor, V_2O_5, presented in Table S7 and Figure S8). The mobility histogram of our 42 devices realized with **ditBu-BTBT** single crystals and its thickness dependence (evaluated by profilometry) is presented in Figure 3e,f. Thinner crystals indeed exhibit higher field-effect mobilities due to the lower access resistance.[17]

The gate-voltage sweep-rate dependence of the nominal mobility of our devices has also been investigated in order to avoid any over-estimation of the extracted values. Chen et al. have recently reported the influence of the gate-voltage sweep-rate in the case of trap dominated FETs exhibiting a dispersive transport.[24] Our devices do not show any significant variation of the extracted mobility for gate-voltage sweeping rates ranging from 0.5 to 19 V s^{-1} (see Figure S9, Supporting Information), confirming the good charge transport performances of **ditBu-BTBT**.

Given the high performances of **ditBu-BTBT** and its good solubility in various solvents, solution-sheared films were fabricated to demonstrate its potential for solution-processed devices. Non-optimized shearing conditions (solution of 2 mg mL^{-1} in tetralin sheared at 0.4 mm s^{-1}) allowed us to produce devices presenting an average mobility of 2.4 $cm^2\ V^{-1}\ s^{-1}$ (maximum mobility of 3.7 $cm^2\ V^{-1}\ s^{-1}$) with ribbon-like crystalline domains in thin films. Optical microscopy images, atomic force microscopy (AFM) images, and FET characteristics of a solution-sheared film are presented in Figure S10 (Supporting Information).

In summary, we have designed and synthesized a series of bulky end-capped BTBTs with the aim of tuning their crystalline packing. A combined theoretical and experimental study allowed us to identify 2,7-di-*tert*-butylBTBT as a new high-performance solution processable OSC with large and well-balanced transfer integrals as evidenced by quantum-chemical calculations. The relevant substitution by two tBu improves the orbital overlap of the molecules within their crystalline architecture. **ditBu-BTBT** PVT grown single-crystal FETs show a remarkable average saturation hole mobility of 7.1 $cm^2\ V^{-1}\ s^{-1}$. Further modifications of the molecular structure of **ditBu-BTBT** aiming to reduce its IP and to improve its molecular packing are currently under investigation.

Experimental Section

Materials: Octadecyltrimethoxysilane (OTS) was purchased from Gelest and used as received (storage under an argon atmosphere to

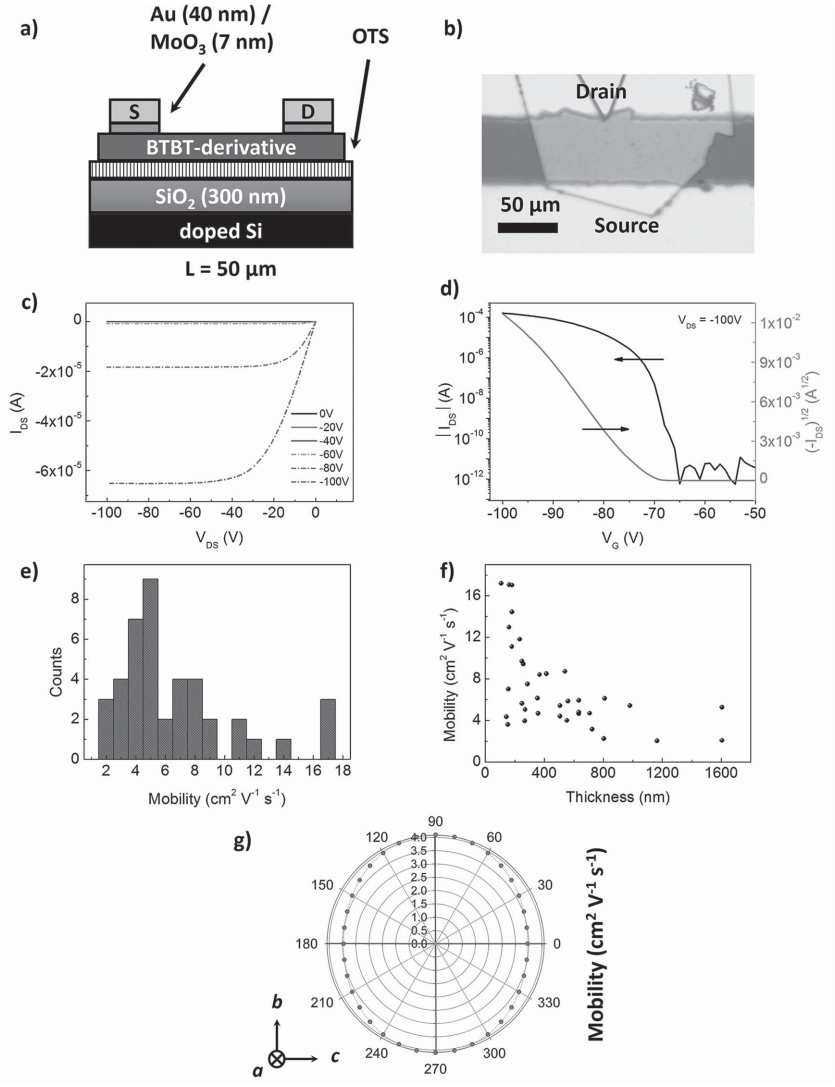

Figure 3. a) Schematic of the bottom-gate top-contact single-crystal device structure (not to scale). b) Optical microscopy image of a **ditBu-BTBT** device presenting a channel width of 124 µm. c,d) Output and transfer (in the saturation regime) characteristics of the depicted device presenting a field-effect mobility of 17 $cm^2\ V^{-1}\ s^{-1}$. e) Mobility histogram of the 42 **ditBu-BTBT** devices. f) Thickness dependence of the field-effect mobility. g) Calculated field-effect mobility anisotropy as a function of the crystallographic orientation for **ditBu-BTBT**.

prevent hydrolysis). Molybdenum (VI) oxide (MoO_3) and vanadium (V) oxide (V_2O_5) were purchased from Aldrich. Highly doped n-type Si (100) wafers (resistivity <0.005 Ω cm, Silicon Quest) were used as the substrates for TFT fabrication. A 300 nm SiO_2 layer (capacitance C_i = 11.5 nF cm^{-2}) was thermally grown onto the Si substrates as a gate dielectric.

Synthesis: The full synthetic procedures of the different bulky end-capped [1]benzothieno[3,2-*b*]benzothiophenes are detailed in the Supporting Information.

Crystal Growth: Single crystals were grown by the physical vapor transport method[25] at atmospheric pressure in a high-purity argon flow of 80 sccm; the details of this setup are described elsewhere.[26] Typical growth conditions (temperatures of the sublimation and growth zone as well as growth durations) are presented in Table S2 (Supporting Information). Crystals varied in thickness from hundreds of nanometers to several micrometers. The thinnest crystals were mainly selected due to their better performances.[26]

Crystal Analysis: For **ditBu-BTBT** and **diTMS-BTBT** (single crystals grown from solution), data collection and processing was carried out on an Oxford diffraction Xcalibur E diffractometer using Mo K_α radiation;[27] for **tBu-BTBT**, **iPr-BTBT**, and **diiPr-BTBT** (single crystals grown by sublimation), data were recorded on a Bruker-Nonius X8 Proteum CCD diffractometer using Cu K_α radiation.[28] The crystal structures were solved using SHELXS and refined by full matrix least-squares methods based on F^2 using SHELXL97 or SHELXL-2014.[29] The displacement parameters of all non-H atoms were treated anisotropically. H atoms were placed at calculated positions using suitable riding models with fixed isotropic thermal parameters [U_{iso}(H) = 1.2U_{eqv}(C) for CH groups and U_{iso}(H) = 1.5U_{eqv}(C) for CH_3]. The relatively high R-values for the vapor-grown crystals, and especially of **tBu-BTBT**, were largely a consequence of poor counting statistics caused by the extreme thinness of the crystals.[30]

CCDC 1008118 (**tBu-BTBT**), 1008119 (**iPr-BTBT**), 1008120 (**diiPr-BTBT**), 1008575, (**ditBu-BTBT**), and 1008576 (**diTMS-BTBT**) contain the supplementary crystallographic data for this paper. These data can be obtained free of charge from The Cambridge Crystallographic Data Centre via www.ccdc.cam.ac.uk/data_request/cif.

Hirshfeld Surface Analysis: Hirshfeld surfaces[31] and the associated fingerprint plots[32] were calculated using Crystal Explorer (Version 3.1),[33] which accepts a structure input file in the CIF format. Bond lengths to hydrogen atoms were set to typical neutron-diffraction values (C–H = 1.083 Å). For each point on the Hirshfeld isosurface, two distances d_e, the distance from the point to the nearest nucleus external to the surface, and d_i, the distance to the nearest nucleus internal to the surface, are defined. The normalized contact distance (d_{norm}) based on d_e and d_i is given by:

$$d_{norm} = \frac{(d_i - r_i^{vdw})}{r_i^{vdw}} + \frac{(d_e - r_e^{vdw})}{r_e^{vdw}} \quad (1)$$

where r_i^{vdW} and r_e^{vdW} are the van der Waals radii of the atoms. The value d_{norm} is negative or positive depending if the intermolecular contacts are shorter or longer than the van der Waals separations. The parameter d_{norm} displays a surface with a red–white–blue color scheme, where bright red spots highlight shorter contacts, white areas represent contacts around the van der Waals separation, and blue regions are devoid of close contacts.

Crystal Growth Morphology Calculation: Crystal growth morphologies were calculated from the solved crystal structures using the Morphology module of the Materials Studio Package[34] (Compass force field).[35] The attachment energy (E_{att}) method developed by Hartman was used to determine the relative importance of the different crystallographic faces in the crystal morphology: faces with higher E_{att} (in absolute value) grow faster and have less importance in the final shape and vice versa.[16] This methodology is quite efficient to describe the shape of crystals grown from vapor or from the melt, i.e., without external interactions (solvent molecule by example).

Single-Crystal Device Fabrication: Due to the deep ionization potential of our BTBT-derivatives, single-crystal devices were fabricated in a bottom-gate-top-contact geometry using a doping agent to improve

the contacts. Freshly grown single crystals were first laminated on OTS treated 300 nm thermally grown SiO_2 substrates. The monolayer was deposited according to a method we published previously.[36] Approximately 7 and 40 nm of molybdenum oxide and gold were thermally evaporated onto the single crystals at a rate of 0.2 and 0.5 Å s^{-1}, respectively, while rotating the substrate holder, to complete the devices. The electrode dimensions were defined by a shadow mask with a 50 µm channel length (L), and a W/L ratio of 20. The W/L used in the mobility calculation for single-crystal devices was evaluated from the individual crystal used (average of the length of each side of the crystal in contact with the electrodes).

Solution-Sheared Device Fabrication: The shearing substrates were prepared using Si wafers with 300 nm SiO_2 layer functionalized with pentafluoro-phenylpropyltrichlorosilane following the procedure described in previous work.[37] Solution shearing was performed as follows. First, 2 mg mL^{-1} **ditBu-BTBT** solution in tetralin was prepared and then sandwiched between the shearing blade and the substrate. The substrate was heated to 133 °C, and the blade was tilted by 8°. The blade front was separated from the substrate surface by 40 µm. The shearing speed was 0.4 mm s^{-1}. The resulting film thickness was 55 nm on average, measured by AFM. Mobility was channel width corrected.[38]

Device Characterization: Transistors were characterized using a Keithley 4200-SCS semiconductor parameter analyzer and standard probe station setup at room temperature in an N_2-filled glovebox. Device parameters were extracted using the standard calculation techniques. The devices were stored in the dark in an N_2-filled glovebox.

Other Characterization Techniques: Optical microscopy images were recorded with a cross-polarized optical microscope (Leica DM4000M). Thickness measurements were realized with a Dektak 150 profilometer (Veeco Metrology Group). Tapping mode atomic force microscopy was performed using a Multimode Nanoscope III (Digital Instruments/Veeco Metrology Group). Differential scanning calorimetry (DSC) and thermogravimetric analysis (TGA) were realized, respectively, on a Perkin–Elmer Diamond 6 DSC and a Perkin–Elmer Pyris 6 TGA. Photoelectron spectroscopy in air measurements were recorded on a Riken Keiki AC-2 photoelectron spectrometer. Specular X-ray diffraction (sXRD) of powders was performed on a Bruker D8 Advance diffractometer, using Cu K_α radiation ($\lambda = 1.5418$ Å), equipped with a MRI (Material Research Instruments) heating stage for temperature-dependent measurements. Diffraction patterns were collected in the scattered angular range between 1.6° and 60° with an angular resolution of 0.02° per step and a typical counting time of 20 s per step, using θ/θ reflection geometry (the source and detector both move from the horizontal sample plane at the same angle θ, that is, in specular reflection conditions). GIXD was performed at beam line 11–3 and 1–5 of Stanford Synchrotron Radiation Lightsource (SSRL) at SLAC National Accelerator Laboratory, Menlo Park, CA, USA. The beam energy was 12.73 keV and the incidence angle of X-ray was 0.12°. X-ray diffraction images were collected on a 2D image plate (MAR345, 2300 × 2300 pixels, effective pixel size = 150 µm). The image plate was placed 400 mm from the sample stage. For single-crystal samples, a rotation stage was employed at beamline 1–5 and the diffraction data were collected at ambient conditions. For thin film samples, a helium chamber and a heated sample stage were used for detecting polymorphic transitions during sample annealing. The data analysis was performed using the WxDiff software and customized unit cell indexing algorithm.[39]

Quantum-Chemical Calculations and Kinetic Monte Carlo Simulations: The hole transport properties of all BTBT derivatives were described using the Marcus–Levich–Jortner formalism. This model assumes that charges are hopping between neighboring molecules and expresses the rate of hole transfer k_{hop} as:[40]

$$k_{hop} = \frac{4\pi^2}{h} J^2 \frac{1}{\sqrt{4\pi\lambda_S k_B T}} \sum_\nu \exp(-S)\frac{S^\nu}{\nu!}\exp\left[-\frac{(\lambda_S + \nu\hbar\omega + \Delta G^\circ)^2}{4\lambda_S k_B T}\right] \quad (2)$$

where S is the Huang–Rhys factor which is related to the internal reorganization energy λ_i ($S = \lambda_i/\hbar\omega$), J the transfer integral, λ_s the external reorganization energy, k_B the Boltzmann constant, T the temperature, ΔG° the free energy of the reaction, and $\hbar\omega$ is an effective vibrational mode (carbon–carbon stretching mode) that assists charge transport. The internal reorganization energy entering the Huang–Rhys factor is a parameter that reflects the geometric changes of the molecules involved in the charge transport process upon charge transfer. It has been evaluated at the DFT level (B3LYP/6-31g**) according to the procedure described elsewhere.[41] The $\hbar\omega$ effective stretching mode was set to 0.2 eV and the external reorganization energy to the typical value of 0.1 eV.[42] The HOMO transfer integral (J) describes the amplitude of the interactions between the HOMO electronic levels of the two molecules involved in the hole transfer process. This term has been estimated in a fragment approach at the DFT level (B3LYP/DZ) with the Amsterdam Density Functional (ADF) package[43] as described elsewhere.[44] Due to the weak energetic disorder in crystals, ΔG° can be expressed solely as $\Delta G^\circ = e\vec{F}\vec{d}$, where $\vec{F}$ and $\vec{d}$ are the electric field and distance vectors between mass centers, respectively. Finally, the charge carrier mobility (μ) was evaluated using a kinetic Monte Carlo technique with the First Reaction Method algorithm. This technique allowed us to propagate of a single charge carrier in the crystals following a stochastic dynamics where the direction taken by the charge in the crystal in each Monte Carlo cycle is chosen according to the smallest hopping time. The hopping time t_{ij} (rate k_{ij}) between two molecules i and j is related to the hopping rates k_{ij} with the following expression:

$$t_{ij} = -\frac{\ln(r)}{k_{ij}} \quad (3)$$

where r is a random number chosen between 0 and 1. The charge carrier mobility is obtained at the end of the simulation as:

$$\mu = \frac{d_{tot}}{t_{tot}F} \quad (4)$$

where d_{tot} and t_{tot} are the total distance travelled during the kinetic Monte Carlo simulation and the total time of the simulation obtained as the sum of the t_{ij} values, respectively.

Supporting Information

Supporting Information is available from the Wiley Online Library or from the author.

Acknowledgements

The authors acknowledge funding support from Department of Energy, Bridging Research Interactions through collaborative Development Grants in Energy (BRIDGE) program under contract DE-FOA-0000654-1588, from the Walloon Region (WCS Project No. 1117306), from the European Commission/Walloon Region (FEDER-Smartfilm RF project), from the Interuniversity Attraction Pole program of the Belgian Federal Science Policy Office (PAI 7/05), from the Programme d'Excellence de la Région Wallonne (OPTI2MAT project), from the Belgian National Fund for Scientific Research (FNRS-Project No. 2.4565.11), from a concerted research action of the French Community of Belgium (ARC Project No. 20061), from the National Science Foundation Division of Materials Research Solid-State Chemistry Program (DMR-1303178) and from the Air Force Office of Scientific Research (FA9550-12-1-0190). Y.G. benefits from a mandate of Francqui Research. G.S. kindly acknowledges postdoctoral fellowship support from the David and Alice van Buuren Funds of the Belgian American Educational Foundation (B.A.E.F.) and from the Fulbright Foundation (Fulbright Research Scholar Fellow). J.C. is an FNRS Research Director.

Received: January 20, 2015
Revised: March 12, 2015
Published online: April 9, 2015

[1] H. Sirringhaus, *Adv. Mater.* **2014**, *26*, 1319.
[2] G. Schweicher, Y. Olivier, V. Lemaur, Y. H. Geerts, *Isr. J. Chem.* **2014**, *54*, 595.
[3] V. C. Sundar, J. Zaumseil, V. Podzorov, E. Menard, R. L. Willett, T. Someya, M. E. Gershenson, J. A. Rogers, *Science* **2004**, *303*, 1644.
[4] H. Minemawari, T. Yamada, H. Matsui, J. Tsutsumi, S. Haas, R. Chiba, R. Kumai, T. Hasegawa, *Nature* **2011**, *475*, 364.
[5] a) A. Briseno, S. Mannsfeld, M. Ling, S. Liu, R. Tseng, C. Reese, M. Roberts, Y. Yang, F. Wudl, Z. Bao, *Nature* **2006**, *444*, 913; b) O. Goto, S. Tomiya, Y. Murakami, A. Shinozaki, A. Toda, J. Kasahara, D. Hobara, *Adv. Mater.* **2012**, *24*, 1117; c) S. Liu, W. Wang, A. Briseno, S. Mannsfeld, Z. Bao, *Adv. Mater.* **2009**, *21*, 1217; d) K. Nakayama, Y. Hirose, J. Soeda, M. Yoshizumi, T. Uemura, M. Uno, W. Li, M. J. Kang, M. Yamagishi, Y. Okada, *Adv. Mater.* **2011**, *23*, 1626; e) L. Jiang, H. Dong, W. Hu, *J. Mater. Chem.* **2010**, *20*, 4994.
[6] M. M. Payne, S. R. Parkin, J. E. Anthony, C.-C. Kuo, T. N. Jackson, *J. Am. Chem. Soc.* **2005**, *127*, 4986.
[7] J. Chen, C. K. Tee, M. Shtein, D. C. Martin, J. Anthony, *Org. Electron.* **2009**, *10*, 696.
[8] H. Ebata, T. Izawa, E. Miyazaki, K. Takimiya, M. Ikeda, H. Kuwabara, T. Yui, *J. Am. Chem. Soc.* **2007**, *129*, 15732.
[9] T. Yamamoto, K. Takimiya, *J. Am. Chem. Soc.* **2007**, *129*, 2224.
[10] a) W. Xie, K. Willa, Y. Wu, R. Häusermann, K. Takimiya, B. Batlogg, C. D. Frisbie, *Adv. Mater.* **2013**, *25*, 3478; b) Y. Yuan, G. Giri, A. L. Ayzner, A. P. Zoombelt, S. C. Mannsfeld, J. Chen, D. Nordlund, M. F. Toney, J. Huang, Z. Bao, *Nat. Commun.* **2014**, *5*, 3005.
[11] a) M. J. Kang, I. Doi, H. Mori, E. Miyazaki, K. Takimiya, M. Ikeda, H. Kuwabara, *Adv. Mater.* **2011**, *23*, 1222; b) K. Takimiya, S. Shinamura, I. Osaka, E. Miyazaki, *Adv. Mater.* **2011**, *23*, 4347; c) K. Takimiya, I. Osaka, T. Mori, M. Nakano, *Acc. Chem. Res.* **2014**, *47*, 1493; d) C. Ruzie, J. Karpinska, A. R. Kennedy, Y. H. Geerts, *J. Org. Chem.* **2013**, *78*, 7741; e) C. Niebel, Y. Kim, C. Ruzié, J. Karpinska, B. Chattopadhyay, G. Schweicher, A. Richard, V. Lemaur, Y. Olivier, J. Cornil, A. R. Kennedy, Y. Diao, W.-Y. Lee, S. Mannsfeld, Z. Bao, Y. H. Geerts, *J. Mater. Chem. C* **2015**, *3*, 674.
[12] a) T. Okamoto, C. Mitsui, M. Yamagishi, K. Nakahara, J. Soeda, Y. Hirose, K. Miwa, H. Sato, A. Yamano, T. Matsushita, *Adv. Mater.* **2013**, *25*, 6392; b) C. Mitsui, T. Okamoto, M. Yamagishi, J. Tsurumi, K. Yoshimoto, K. Nakahara, J. Soeda, Y. Hirose, H. Sato, A. Yamano, *Adv. Mater.* **2014**, *26*, 4546.
[13] C. Reese, M. E. Roberts, S. R. Parkin, Z. Bao, *Adv. Mater.* **2009**, *21*, 3678.
[14] C. Reese, M. E. Roberts, S. R. Parkin, Z. Bao, *Appl. Phys. Lett.* **2009**, *94*, 202101.
[15] A. Kreyes, A. Mourran, Z. Hong, J. Wang, M. Möller, F. Gholamrezaie, W. C. Roelofs, D. M. de Leeuw, U. Ziener, *Chem. Mater.* **2013**, *25*, 2128.
[16] P. Hartman, P. Bennema, *J. Cryst. Growth* **1980**, *49*, 145.
[17] H. Jiang, K. J. Tan, K. K. Zhang, X. Chen, C. Kloc, *J. Mater. Chem.* **2011**, *21*, 4771.
[18] Y. Yamagishi, K. Noda, K. Kobayashi, H. Yamada, *J. Phys. Chem. C* **2015**, *119*, 3006.
[19] a) A. Troisi, G. Orlandi, *Phys. Rev. Lett.* **2006**, *96*, 086601; b) M. Hultell, S. Stafström, *Chem. Phys. Lett.* **2006**, *428*, 446.
[20] a) Y. Li, V. Coropceanu, J.-L. Brédas, *J. Phys. Chem. Lett.* **2012**, *3*, 3325; b) A. S. Eggeman, S. Illig, A. Troisi, H. Sirringhaus, P. A. Midgley, *Nat. Mater.* **2013**, *12*, 1045; c) L. Viani, C. Risko, M. F. Toney, D. W. Breiby, J.-L. Brédas, *ACS Nano* **2014**, *8*, 690.
[21] S. M. Ryno, C. Risko, J.-L. Brédas, *J. Am. Chem. Soc.* **2014**, *136*, 6421.
[22] M. C. Gwinner, R. D. Pietro, Y. Vaynzof, K. J. Greenberg, P. K. Ho, R. H. Friend, H. Sirringhaus, *Adv. Funct. Mater.* **2011**, *21*, 1432.
[23] C. Mitsui, J. Soeda, K. Miwa, H. Tsuji, J. Takeya, E. Nakamura, *J. Am. Chem. Soc.* **2012**, *134*, 5448.
[24] Y. Chen, B. Lee, H. Yi, S. Lee, M. Payne, S. Pola, C.-H. Kuo, Y.-L. Loo, J. Anthony, Y. Tao, *Phys. Chem. Chem. Phys.* **2012**, *14*, 14142.
[25] H. Jiang, C. Kloc, *MRS Bull.* **2013**, *38*, 28.
[26] C. Reese, W.-J. Chung, M.-m. Ling, M. Roberts, Z. Bao, *Appl. Phys. Lett.* **2006**, *89*, 202108.
[27] *Oxford Diffraction "CrysAlisPro"*, Yarnton, UK **2010**.
[28] *Bruker-"APEX2"*, Bruker AXS Inc., Madison, WI, USA **2012**.
[29] G. M. Sheldrick, *Acta Crystallogr. Sect. A: Found. Crystallogr.* **2008**, *64*, 112.
[30] S. Parkin, *Acta Crystallogr. Sect. A: Found. Crystallogr.* **2000**, *56*, 157.
[31] F. Hirshfeld, *Theor. Chim. Acta.* **1977**, *44*, 129.
[32] M. A. Spackman, J. J. McKinnon, *CrystEngComm* **2002**, *4*, 378.
[33] CrystalExplorer (Version 3.1), University of Western Australia, Australia **2012**.
[34] *Materials-Studio-Modeling*, Accelrys Software Inc., San Diego, CA, USA **2009**.
[35] H. Sun, *J. Phys. Chem. B* **1998**, *102*, 7338.
[36] Y. Ito, A. A. Virkar, S. Mannsfeld, J. H. Oh, M. Toney, J. Locklin, Z. Bao, *J. Am. Chem. Soc.* **2009**, *131*, 9396.
[37] L. Patrone, V. Gadenne, S. Desbief, *Langmuir* **2010**, *26*, 17111.
[38] H. Li, B. C. K. Tee, J. J. Cha, Y. Cui, J. W. Chung, S. Y. Lee, Z. Bao, *J. Am. Chem. Soc.* **2012**, *134*, 2760.
[39] S. C. B. Mannsfeld, M. L. Tang, Z. Bao, *Adv. Mater.* **2011**, *23*, 127.
[40] V. Coropceanu, J. Cornil, D. da Silva Filho, Y. Olivier, R. Silbey, J. Bredas, *Chem. Rev.* **2007**, *107*, 926.
[41] V. Lemaur, D. da Silva Filho, V. Coropceanu, M. Lehmann, Y. Geerts, J. Piris, M. Debije, A. van de Craats, K. Senthilkumar, L. Siebbeles, *J. Am. Chem. Soc.* **2004**, *126*, 3271.
[42] N. G. Martinelli, J. Idé, R. S. Sánchez-Carrera, V. Coropceanu, J.-L. Brédas, L. Ducasse, F. Castet, J. Cornil, D. Beljonne, *J. Phys. Chem. C* **2010**, *114*, 20678.
[43] G. Te Velde, F. M. Bickelhaupt, E. J. Baerends, C. Fonseca Guerra, S. J. van Gisbergen, J. G. Snijders, T. Ziegler, *J. Comput. Chem.* **2001**, *22*, 931.
[44] a) E. F. Valeev, V. Coropceanu, D. A. da Silva Filho, S. Salman, J.-L. Brédas, *J. Am. Chem. Soc.* **2006**, *128*, 9882; b) L. Viani, Y. Olivier, S. Athanasopoulos, D. A. da Silva Filho, J. Hulliger, J. L. Brédas, J. Gierschner, J. Cornil, *Chem. Phys. Chem.* **2010**, *11*, 1062.